JEECS (Journal of Electrical Engineering and Computer Sciences)
Vol. 11, No. 2, December 2026, pp. 183-195
e-ISSN: 2579-5392 p-ISSN: 2528-0260

Coherence-Gated Set-Membership Recursive Spectral Cancellation for Pulsed Receivers Under Nonstationary Multicomponent Interference

Vu Quang Luong[1], Trinh Thi Minh[2], Bui Kieu Trong Hoang[3]

[1] Missile Faculty, Air Defence-Air Force Academy, Doai Phuong, Hanoi, Vietnam.

[2] Basic Sciences Faculty, Air Defence-Air Force Academy, Doai Phuong, Hanoi, Vietnam.

[3] Battalion 5, Air Defence-Air Force Academy, Doai Phuong, Hanoi, Vietnam.

Article Info

Article history:
Received: 1 August 2026
Revised: 13 October 2026
Accepted: 1 November 2026

Keyword:
Adaptive spectral cancellation
Coherence gating
Nonstationary interference
Pulsed receiver
Set-membership filtering

Abstract

Nonstationary multicomponent interference can obscure weak returns in pulsed receivers. However, broadband reference weighting does not resolve the combined need for frequency-dependent reference reliability, pulse-protected identification, and selective adaptation under unequal auxiliary-channel quality. This simulation study proposes a coherence-gated set-membership recursive spectral canceller (CG-SM-RSC). It combines guarded short-time Fourier identification, frequency-bin coherence weighting, a regularized two-input Wiener solution, weighted overlap-add synthesis, and residual-driven covariance updates. Pulse-bearing and guard samples are excluded from identification while synthesis remains active. Ten deterministic Monte Carlo runs per operating level compare CG-SM-RSC with time-domain normalized least-mean-square filtering, recursive spectral cancellation, and ungated set-membership spectral cancellation. CG-SM-RSC achieves the highest off-pulse cancellation among these baselines in the moderate and severe cases, at 11.852 and 10.563 dB. In the favorable case, it achieves 10.300 dB with a 12.1% covariance-update ratio, although time-domain filtering gives higher cancellation. These results indicate a condition-dependent benefit from frequency-resolved gating and selective updates. The evaluation uses synthetic signals; no prototype or measured-receiver validation is reported.

Corresponding author:
Vu Quang Luong, vuquangluong88@gmail.com

DOI: https://doi.org/10.54732/jeecs.v11i2.8

This is an open access article under the CC–BY license.

1. Introduction

Pulsed radar and communication receivers increasingly operate in congested electromagnetic environments containing narrowband emitters, multitone signals, frequency-wandering carriers, and asynchronous bursts. These disturbances raise the spectral floor, mask weak returns, and bias subsequent detection or estimation. Recent radar studies have therefore examined the interference phenomenology and receiver-side reconstruction problem [1], [2], [3].

Model-based methods exploit different structures in corrupted FMCW observations. Matrix-pencil estimation reconstructs parametric signal component [4], whereas sparse and low-rank Hankel decomposition separates components through structural constraints [5]. Iterative two-dimensional recovery uses masked residual update [6], and time-domain synthesis reconstructs the estimated interference waveform [7]. These approaches motivate structured reconstruction, but their FMCW formulations do not directly specify how two unequal auxiliary references should be weighted while pulse-bearing samples are withheld from identification.

Other approaches exploit temporal or transform-domain structure. MTI-like processing uses inter-chirp behavior [8], while multiplicative-adaptive filtering combines adaptive processing with a Hilbert-

transform representation [9]. Time-frequency and dual-domain fusion provide another separation strategy [10]. Variational separation [11], support-vector methods [12], and VMD with VI-CFAR processing [13] use different models of interference structure. For the pulsed-receiver problem considered here, these studies provide relevant context but do not constitute the matched auxiliary-channel baselines evaluated in this paper.

Adaptive cancellation remains attractive when auxiliary channels observe correlated versions of the disturbance. Time-domain filter order selection and notch-based suppression have been studied for navigation and communication receivers [14], [15]. General adaptive-filtering theory explains the trade-off among tracking, misadjustment, conditioning, and computational load [16]. Set-membership algorithms reduce updates by enforcing a bounded residual, and robust error criteria can improve behavior under impulsive contamination [17], [18], [19]. Radar interference surveys describe a broad range of mitigation strategies [20], and adaptive noise cancellation demonstrates the value of correlated reference observations [21]. Learning-based reconstruction [22] and spectrum-subband analysis and synthesis [23] offer additional ways to retain useful signal content.

Recent work further illustrates the distinction between reconstruction and reference-based cancellation. Thornton et al. presented a temporal convolutional autoencoder for FMCW radar altimeters [24], explicitly identifying generalization and real-time feasibility as open issues. Joshani et al. investigated two-dimensional autoregressive interference mitigation for FMCW radar [25]. These studies concern FMCW reconstruction and are included as current context, not as numerical baselines. Their results cannot be ranked directly against the present pulsed-receiver simulations because the observation models and evaluation protocols differ.

However, a joint design issue remains for the pulsed-receiver setting considered here: frequency-dependent reliability in two unequal auxiliary references must be handled while target-bearing samples are excluded from identification and covariance updates are performed selectively. The specific research gap is the coordinated treatment of these requirements within a common spectral cancellation framework, with cancellation remaining active during pulse intervals. This requires a matched evaluation of the resulting trade-offs among interference suppression, target projection, and update frequency.

To address this gap, this paper develops CG-SM-RSC for the pulsed-receiver setting. The framework combines guarded spectral identification, independent coherence gates for two references, a regularized two-input Wiener solution, and a set-membership update controller. The contribution is the integration and simulation evaluation of these mechanisms; the individual mechanisms are not claimed to be new. The evaluation compares three operating scenarios and examines parameter sensitivity. The comparisons assess cancellation, target projection, and covariance-update frequency; they do not establish hardware latency or universal superiority over the wider literature.

The paper is structured as follows. Section 2 presents the signal and interference model, the proposed cancellation framework, and the simulation methodology. Section 3 provides a comparative performance analysis and discusses parameter sensitivity and the main findings. Section 4 concludes the study, addressing its limitations and directions for future research.

2. Research Methodology

2.1. Signal and interference model

2.1.1. Pulse gate and target component

The repetition interval and pulse width are represented by the binary pulse gate:

$$g[n]=\begin{cases}1, & 0\le \mathrm{mod}(n,N_R)<N_P\\ 0, & \text{otherwise}\end{cases} \tag{1}$$

where n is the sample index, N_R is the repetition-interval sample count, and N_P is the pulse-width sample count.

A nontrivial complex target is generated to evaluate pulse preservation:

$$s[n]=A_s g[n]\exp\left\{j\left(2\pi f_D\frac{n}{F_s}+\pi\kappa_D\left(\frac{n}{F_s}\right)^2+\beta_D\sin\left(2\pi f_m\frac{n}{F_s}\right)\right)\right\} \tag{2}$$

where A_s is target amplitude, F_s is sampling frequency, f_D is Doppler frequency, κ_D is the quadratic phase coefficient, β_D is the micro-phase depth, and f_m is its modulation frequency.

2.1.2. Nonstationary multicomponent interference

The slowly varying disturbance envelope is defined as:

$$a[n]=1+m_1\cos\left(2\pi f_{a1}\frac{n}{F_s}+\theta_1\right)+m_2\cos\left(2\pi f_{a2}\frac{n}{F_s}+\theta_2\right) \tag{3}$$

where m_1 and m_2 are modulation depths, f_{a1} and f_{a2} are envelope frequencies, and θ_1 and θ_2 are initial phases.

The phase of the m-th interference component includes carrier wander and chirp:

$$\varphi_m[n]=2\pi f_m\frac{n}{F_s}+\frac{\Delta f_m}{f_{wm}}\sin\left(2\pi f_{wm}\frac{n}{F_s}+\varphi_m\right)+\pi\nu_m\left(\frac{n}{F_s}\right)^2 \tag{4}$$

where f_m is nominal frequency, Δf_m is wander amplitude, f_{wm} is wander frequency, φ_m is wander phase, and ν_m is chirp rate.

The complete source disturbance is power-normalized as:

$$u[n]=\frac{a[n]\sum_{m=1}^{M}c_m\exp\{j\phi_m[n]\}}{\sqrt{\mathrm{E}\left\{\left|a[n]\sum_{m=1}^{M}c_m\exp\{j\phi_m[n]\}\right|^2\right\}}} \tag{5}$$

where M is the component count and c_m is the complex coefficient of component m.

2.1.3. Main and auxiliary observations

Distinct multipath responses create frequency-dependent mismatch among receivers:

$$j_k[n]=\sum_{q=0}^{Q_k-1}h_{k,q}u[n-d_{k,q}],\qquad k\in\{1,2,3\} \tag{6}$$

where $h_{k,q}$ and $d_{k,q}$ are the complex gain and integer delay of path q in channel k, respectively.

The main and two auxiliary observations are modeled by:

$$\rho_k[n]=\mathrm{clip}_{[\rho_{\min},\rho_{\max}]}\left(\bar{\rho}_k+\Delta\rho_k\sin\left(2\pi f_{\rho k}\frac{n}{F_s}+\psi_k\right)\right) \tag{7}$$

and the three observations are:

$$\begin{aligned}y[n]&=s[n]+A_j j_1[n]+v_1[n]\\ x_k[n]&=A_j\left(\rho_k[n]j_k[n]+\sqrt{1-\rho_k^2[n]}q_k[n]\right)+v_k[n]+b_k[n]+\ell_k s[n],\quad k=2,3\end{aligned} \tag{8}$$

where A_j is interference amplitude, $\rho_k[n]$ is time-varying reference correlation, $q_k[n]$ is an independent disturbance, $v_k[n]$ is complex Gaussian noise, $b_k[n]$ is burst contamination, and ℓ_k is target leakage.

Target-bearing samples and their pulse-edge guards are excluded from identification through:

$$\chi[n]=\prod_{r=-N_G}^{N_G}\left(1-g[n-r]\right) \tag{9}$$

where N_G is the number of guard cells on each side of a pulse. Samples with $\chi[n]=0$ are retained in the synthesis path but excluded from identification.

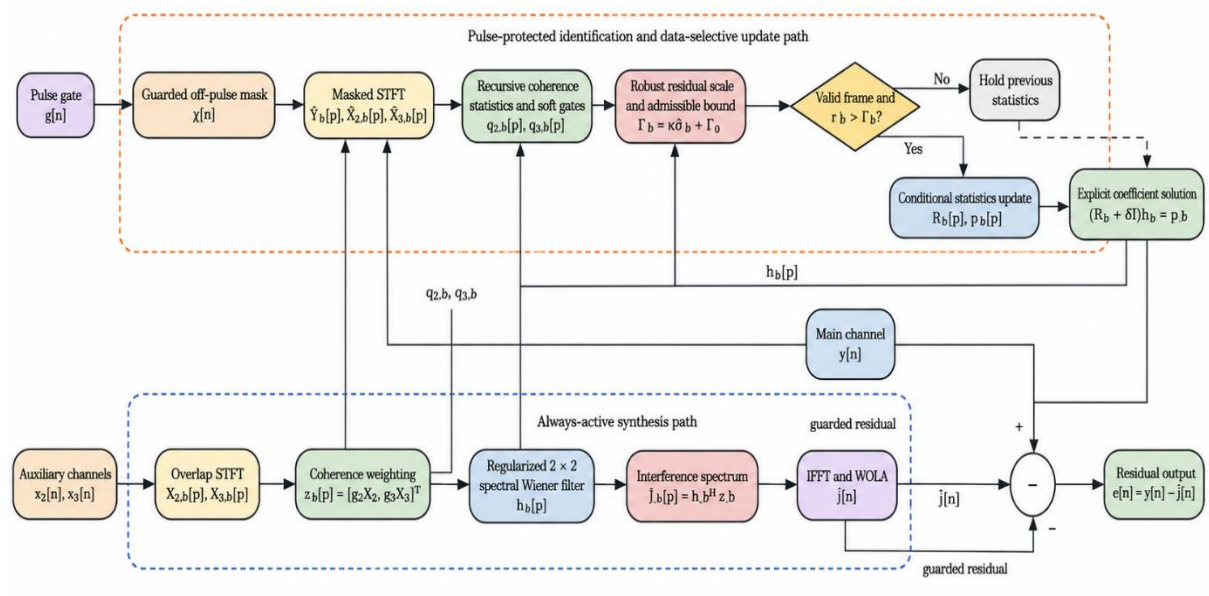

Figure 1. Complete processing flow of the proposed CG-SM-RSC algorithm

2.2. CG-SM-RSC processing algorithm

Figure 1 separates the always-active synthesis path from the pulse-protected identification and data-selective update path. The auxiliary spectra are used continuously to synthesize an interference estimate, whereas the guarded spectra update coherence and Wiener statistics only when a valid off-pulse residual exceeds the adaptive bound. The two paths exchange frequency-bin reliability gates and recursively estimated coefficients. This arrangement preserves cancellation during target-bearing intervals without adapting the model to the desired pulse.

For frame index b, the overlapping sample set starts at:

$$n_b = bH, \qquad \mathrm{I}_b = \{n_b, n_b+1, \ldots, n_b+B-1\} \tag{10}$$

where B is frame length and H is hop size. Using a square-root Hann window $w[r]$, the synthesis short-time Fourier transform is:

$$X_{k,b}[p] = \sum_{r=0}^{B-1} w[r]x_k[n_b+r]\exp\left(-j\frac{2\pi pr}{B}\right) \tag{11}$$

where p is the frequency-bin index. The identification spectra are computed with the guarded mask:

$$\tilde{X}_{k,b}[p] = \sum_{r=0}^{B-1} w[r]\chi[n_b+r]x_k[n_b+r]\exp\left(-j\frac{2\pi pr}{B}\right) \tag{12}$$

where the tilde denotes a pulse-protected spectrum; $\tilde{Y}_b[\mathrm{p}]$ is defined identically for the main channel.

2.3. Frequency-bin coherence gates

The guarded main-channel power is recursively tracked by:

$$S_{yy,b}[p] = \lambda_c S_{yy,b-1}[p] + (1-\lambda_c)\left|\tilde{Y}_b[p]\right|^2 \tag{13}$$

where λ_c is the coherence-statistics forgetting factor. Reference powers and main-reference cross spectra obey:

$$\begin{aligned} S_{x_k x_k,b}[p] &= \lambda_c S_{x_k x_k,b-1}[p] + (1-\lambda_c)\left|\tilde{X}_{k,b}[p]\right|^2, \\ S_{yx_k,b}[p] &= \lambda_c S_{yx_k,b-1}[p] + (1-\lambda_c)\tilde{Y}_b[p]\tilde{X}^*_{k,b}[p] \end{aligned} \tag{14}$$

where $(\cdot)^*$ denotes complex conjugation. The magnitude-squared coherence is estimated independently for each reference and bin:

$$\gamma_{k,b}^2[p] = \mathrm{clip}_{[0,1]}\left\{\frac{\left|S_{yx_k,b}[p]\right|^2}{S_{yy,b}[p]S_{x_kx_k,b}[p]+\varepsilon}\right\} \tag{15}$$

where ε is a small positive regularization constant. Coherence is mapped to a soft reliability gate:

$$q_{k,b}[p] = q_0 + (1-q_0)\left\{\mathrm{clip}_{[0,1]}\left[\frac{\gamma_{k,b}^2[p]-\gamma_{\min}}{1-\gamma_{\min}}\right]\right\}^{\xi}, \tag{16}$$
$$g_{k,b}[p] = \sqrt{q_{k,b}[p]}$$

where q_0 retains a minimum information path, $\gamma_{\min}$ is the useful-coherence threshold, and ξ controls transition sharpness. The weighted two-reference vector supplied to the canceller is:

$$\mathbf{z}_b[p] = \begin{bmatrix} g_{2,b}[p]X_{2,b}[p] \\ g_{3,b}[p]X_{3,b}[p] \end{bmatrix} \tag{17}$$

where $(\mathrm{g})^T$ denotes vector transpose.

2.4. Recursive spectral Wiener solution and synthesis

The frequency-bin covariance matrix is updated as:

$$\mathbf{R}_b[p] = \lambda_r \mathbf{R}_{b-1}[p] + (1-\lambda_r)\alpha_b \tilde{\mathbf{z}}_b[p]\tilde{\mathbf{z}}_b^H[p] \tag{18}$$

where λ_r is the covariance forgetting factor, α_b is the set-membership update coefficient, $\tilde{\mathbf{z}}_b[p]$ is formed from guarded spectra, and $(\mathrm{g})^H$ denotes Hermitian transpose.

The associated cross-correlation vector is:

$$\mathbf{p}_b[p] = \lambda_r \mathbf{p}_{b-1}[p] + (1-\lambda_r)\alpha_b \tilde{\mathbf{z}}_b[p]\tilde{Y}_b^*[p] \tag{19}$$

where $\mathbf{p}_b[p]$ contains the two main-reference correlations. The regularized per-bin Wiener criterion is:

$$J_b(\mathbf{h}) = \mathrm{E}\left\{\left|\tilde{Y}_b[p] - \mathbf{h}^H[p]\tilde{\mathbf{z}}_b[p]\right|^2\right\} + \delta\left\|\mathbf{h}[p]\right\|_2^2 \tag{20}$$

where δ is diagonal loading and $\mathbf{h}[p]$ is the coefficient vector. Minimizing (20) yields the two-input normal equation:

$$\left(\mathbf{R}_b[p] + \delta\mathbf{I}_2\right)\mathbf{h}_b[p] = \mathbf{p}_b[p] \tag{21}$$

where I_2 is the 2×2 identity matrix. The determinant used by the explicit coefficient solution is:

$$\Delta_b[p] = \left(R_{22,b}[p]+\delta\right)\left(R_{33,b}[p]+\delta\right) - \left|R_{23,b}[p]\right|^2 \tag{22}$$

where R_{22}, R_{33}, and R_{23} are entries of $\mathbf{R}_b[p]$. The two coefficients are evaluated without a general matrix inversion:

$$h_{2,b}[p] = \frac{\left(R_{33,b}[p]+\delta\right)p_{2,b}[p] - R_{23,b}[p]p_{3,b}[p]}{\Delta_b[p]+\varepsilon},$$
$$h_{3,b}[p] = \frac{-R_{23,b}^*[p]p_{2,b}[p] + \left(R_{22,b}[p]+\delta\right)p_{3,b}[p]}{\Delta_b[p]+\varepsilon} \tag{23}$$

where all quantities in (23) are evaluated at bin p. The interference spectrum is synthesized from the gated references:

$$\hat{J}_b[p] = h_{2,b}^*[p]g_{2,b}[p]X_{2,b}[p] + h_{3,b}^*[p]g_{3,b}[p]X_{3,b}[p] \tag{24}$$

where $\hat{J}_b[p]$ is the frame interference estimate. Inverse transformation and weighted overlap-add produce a continuous estimate and residual:

$$\hat{j}[n] = \frac{\sum_b w[n-bH]\hat{j}_b[n-bH]}{\sum_b w^2[n-bH]+\varepsilon}, \quad e[n] = y[n] - \hat{j}[n] \tag{25}$$

where $\hat{j}[n]$ is the inverse-transform frame and $e[n]$ is the canceller output.

2.5. Set-membership update control

A burst-resistant residual scale is tracked from guarded samples:

$$\hat{\sigma}_b = \lambda_\sigma \hat{\sigma}_{b-1} + (1-\lambda_\sigma)\min\left\{\frac{\text{median}_{\chi=1}\left|w[r]e[n_b+r]\right|}{\sqrt{\ln 2}}, \sigma_{\max}\right\} \tag{26}$$

where λ_σ is the scale forgetting factor and $\sigma_{\max}$ prevents a burst from inflating the estimate. The admissible frame-error bound is:

$$\Gamma_b = \kappa\hat{\sigma}_b + \Gamma_0 \tag{27}$$

where κ is the bound factor and Γ_0 is a nonzero floor. The guarded frame residual magnitude is:

$$r_b = \sqrt{\frac{\sum_{r\in\Omega_b} w^2[r]\left|e[n_b+r]\right|^2}{|\Omega_b|+\varepsilon}}, \Omega_b = \{r : \chi[n_b+r]=1\} \tag{28}$$

where Ω_b is the valid off-pulse sample set in frame b. The data-selective update coefficient is:

$$\alpha_b = \max\left\{0, 1-\frac{\Gamma_b}{r_b+\varepsilon}\right\} \tag{29}$$

so the covariance statistics are held when the residual lies inside the admissible set. The approximate implementation load is dominated by FFT/IFFT operations and per-bin arithmetic:

$$C \approx \frac{6B\log_2 B + B + \kappa_a B}{H} \quad \text{complex operations/sample} \tag{30}$$

where κ_a groups fixed two-input arithmetic per frequency bin.

2.6. Simulation design and performance criteria

Table 1 summarizes the main signal and algorithm parameters used in the simulations, including pulse timing, spectral analysis settings, recursive tracking parameters, regularization, and the thresholds governing coherence gating and selective updates.

Table 1. Main signal and algorithm parameters

Parameter	Symbol	Value	Role
Sampling frequency	F_s	1 MHz	Digital sampling rate
Record length	N	12,288	Simulated samples
Pulse repetition frequency	PRF	20 kHz	Pulse timing
Pulse width	T_p	4 μs	Target-bearing interval
Frame length	B	256 samples	STFT resolution
Hop size	H	128 samples	50% overlap
Covariance forgetting	λ_r	0.94	Spectral tracking
Coherence forgetting	λ_c	0.92	Reliability smoothing
Diagonal loading	δ	2×10^{-3}	Conditioning
Coherence threshold	$\gamma_{\min}$	0.12	Reject weak bins
Error-bound factor	κ	1.55	Update control
Pulse guard	N_G	3 samples	Pulse-edge protection

Table 2. Three evaluation parameter sets

Set	Operating level	JNR (dB)	ρ_2; ρ_3	Max. wander (kHz)	Burst probability	Burst amplitude	Target leakage
S1	Favorable	15	0.97; 0.94	1.2	0.0001	8	0.002
S2	Moderate	25	0.89; 0.80	7.0	0.0010	18	0.008
S3	Severe	35	0.75; 0.62	18.0	0.0040	30	0.020

Each comparison entry is averaged over ten deterministic Monte Carlo runs using synthetic observations; no hardware prototype or measured-receiver experiment is included. S1, S2, and S3 denote the favorable, moderate, and severe simulation parameter sets defined in Table 2. They are author-defined scenarios, not methods or datasets taken from references. The baselines are a two-reference 10-tap/channel TD-NLMS filter, based on the standard adaptive-filtering framework [16], and two internal spectral ablations: always-updated RSC and SM-RSC without coherence gating. The latter variants isolate the update-control and gating components of the present framework; they are not claimed as reproduced implementations of separate published papers. All methods use identical observations and pulse masks.

The principal off-pulse cancellation factor is:

$$C_{\text{off}} = 10\log_{10}\left\{\frac{\sum_{n\in\text{off}} \left|A_j\, j_1[n]\right|^2 + \varepsilon}{\sum_{n\in\text{off}} \left|e[n]\right|^2 + \varepsilon}\right\} \tag{31}$$

where off denotes guarded non-pulse samples. Average spectral-peak attenuation is calculated by:

$$A_{\text{peak}} = \frac{1}{M}\sum_{m=1}^{M} 10\log_{10}\left\{\frac{\max_{f\in B_m} S_y(f)}{\max_{f\in B_m} S_e(f) + \varepsilon}\right\} \tag{32}$$

where B_m is the analysis band around component m, and $S_y(f)$ and $S_e(f)$ are input and residual power spectra. The corresponding average band-energy attenuation is:

$$A_{\text{band}} = \frac{1}{M}\sum_{m=1}^{M} 10\log_{10}\left\{\frac{\int_{B_m} S_y(f)df}{\int_{B_m} S_e(f)df + \varepsilon}\right\} \tag{33}$$

where the integrals are evaluated numerically over each disturbance band. Target-component preservation is measured through projection gain:

$$G_t = 20\log_{10}\left\{\frac{\left|\mathbf{s}^H\mathbf{e}\right|}{\mathbf{s}^H\mathbf{s} + \varepsilon}\right\} \tag{34}$$

where a value close to 0 dB indicates negligible target distortion. The computational benefit of set-membership control is summarized by:

$$R_{\text{up}} = \frac{N_{\text{update}}}{N_{\text{frame}}} \tag{35}$$

where N_{update} is the number of covariance updates and Nframe is the number of processed frames.

3. Results and Discussions

3.1. Waveform, spectrum, and convergence

The moderate case combines unequal reference correlations, sparse high-amplitude bursts, and target leakage. Figure 2 shows that the amplitude-modulated off-pulse interference is strongly reduced after the initial frames while short peaks remain at target positions. This behavior follows directly from the guarded identification mask: the target and pulse-edge samples do not modify the recursive statistics, but the synthesis path continues to generate an interference estimate throughout the record.

The severe case contains broad spectral regions generated by frequency wander, chirp, and envelope modulation. Figure 3 confirms attenuation around all three principal frequencies. The residual is nonuniform because the auxiliary-channel correlations are frequency dependent; bins for which both references are weakly coherent receive small gates and therefore contribute less to the estimate. This controlled reduction is preferable to unstable amplification of corrupted reference bins.

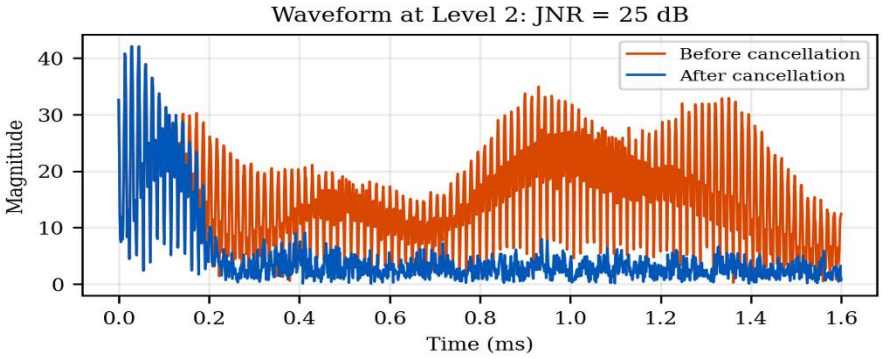

Figure 2. Main-input and CG-SM-RSC residual magnitudes for the moderate parameter set S2

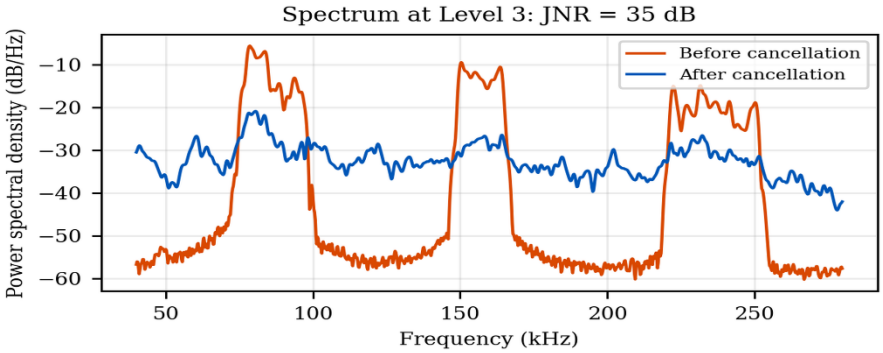

Figure 3. Power spectral densities before and after cancellation for the severe parameter set S3

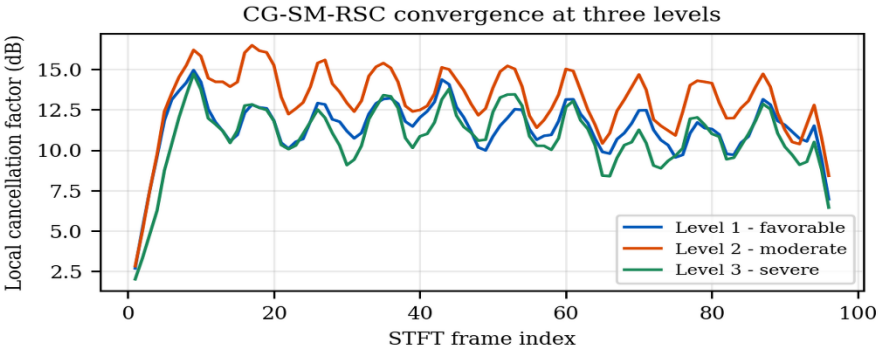

Figure 4. Local CG-SM-RSC cancellation factor for the three operating levels

Figure 4 compares the framewise convergence behavior. All three curves rise during the initial adaptation interval and then fluctuate with nonstationary interference power and reference correlation. The favorable set is smoothest, whereas the severe set exhibits deeper local reductions without persistent divergence. The combination of diagonal loading, coherence gating, and bounded updates prevents the covariance recursion from following isolated burst-dominated bins.

Table 3. Monte Carlo comparison across author-defined scenarios S1–S3

Scenario	Method	Coff (dB)	Apeak (dB)	Aband (dB)	Gt (dB)	Rup
S1	TD-NLMS [16]	12.273±0.063	24.219	19.584	-0.166	100.0%
S1	RSC	10.867±0.053	21.105	16.792	-0.059	100.0%
S1	SM-RSC	9.778±0.194	16.081	13.873	0.055	13.1%
S1	CG-SM-RSC	10.300±0.258	16.469	14.525	0.020	12.1%
S2	TD-NLMS [16]	11.399±0.067	17.664	15.947	1.144	100.0%
S2	RSC	11.532±0.038	17.368	15.743	0.487	100.0%

Scenario	Method	Coff (dB)	Apeak (dB)	Aband (dB)	Gt (dB)	Rup
S2	SM-RSC	11.471±0.040	17.325	15.672	0.498	100.0%
S2	CG-SM-RSC	11.852±0.052	17.902	16.063	0.706	100.0%
S3	TD-NLMS [16]	7.325±0.110	10.545	10.584	-0.678	100.0%
S3	RSC	9.902±0.098	12.845	12.069	-1.745	100.0%
S3	SM-RSC	9.896±0.097	12.860	12.073	-1.725	100.0%
S3	CG-SM-RSC	10.563±0.093	13.688	12.931	-1.561	100.0%

3.2. Quantitative comparison

Notes: S1 = favorable, S2 = moderate, and S3 = severe; their parameter values are defined in Table 2 and have no external reference numbers. TD-NLMS uses the standard framework in [16]. RSC and SM-RSC are internal ablation baselines described in Section 2.6; CG-SM-RSC is the proposed method. All tabulated values are from the present simulation study, not imported from the cited literature.

Table 3 and Figure 5 show that the benefit depends on the operating scenario. In S2, CG-SM-RSC achieves 11.852 dB off-pulse cancellation, exceeding TD-NLMS, RSC, and SM-RSC by 0.453, 0.320, and 0.381 dB, respectively. In S3, the corresponding gains are 3.238, 0.661, and 0.667 dB. These comparisons support improved mean cancellation under the moderate and severe simulated conditions. In S1, TD-NLMS reaches 12.273 dB compared with 10.300 dB for CG-SM-RSC, so the proposed method is not the strongest canceller in that scenario. Its S1 advantage is selective adaptation: the covariance-update ratio is 12.1%, corresponding to 87.9% fewer updated frames than an always-updated spectral baseline. This is an update-count reduction, not a measured 87.9% reduction in runtime or energy.

In S2 and S3, CG-SM-RSC also has the highest spectral-peak and band-energy attenuation among the four tested methods. In S3, it reaches 13.688 dB peak attenuation and 12.931 dB band attenuation. Target projection does not follow the same ranking: the proposed method gives 0.706 dB in S2 and −1.561 dB in S3, whereas other methods yield values closer to zero. The guarded mask prevents pulse-bearing samples from entering identification, but it does not by itself prove distortion-free synthesis when target leakage is present. Residual interference and target distortion can both affect the projection metric; the reported results do not separately quantify these contributions.

3.3. Parameter sensitivity and operating domain

Table 4 summarizes the one-factor sensitivity results for frame length in S2, the coherence threshold in S3, and the error-bound factor in S1. These sweeps characterize how each parameter affects cancellation, spectral-peak attenuation, and the covariance-update ratio at the selected operating points.

Frame length controls the time-frequency resolution and the number of independent updates. Figure 6 shows that increasing B from 128 to 256 slightly decreases Coff but improves spectral-peak attenuation because the frequency bins better isolate the three disturbance regions. A 512-sample frame loses tracking capability under the imposed wander. The selected B=256 and H=128 therefore provide the best compromise between spectral selectivity and nonstationary tracking for this data set.

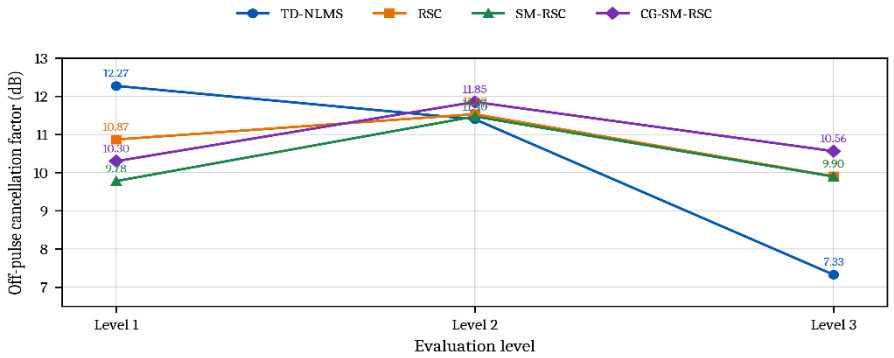

Figure 5. Off-pulse cancellation factor of the four methods across the three operating levels

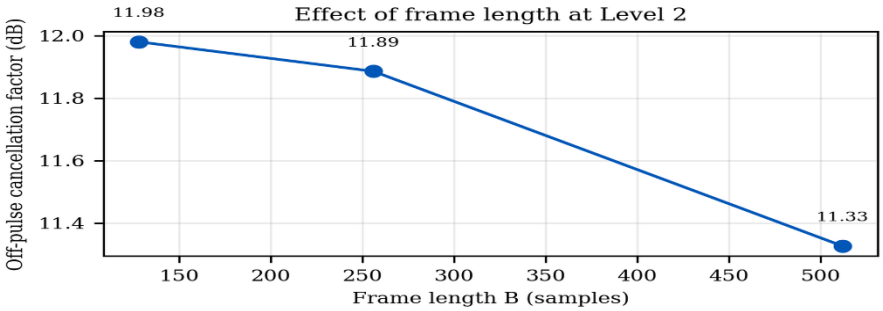

Figure 6. Effect of frame length on the moderate operating level S2

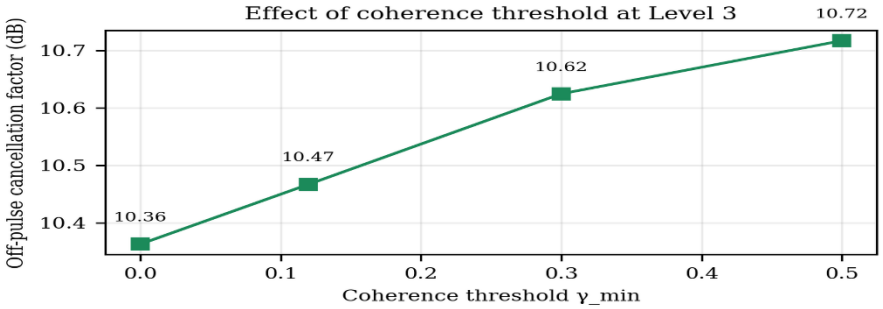

Figure 7. Effect of the coherence threshold on the severe operating level S3

The coherence threshold determines how strongly low-predictability bins are suppressed. Figure 7 shows a monotonic improvement from γ_{min}=0 to 0.50 in the severe case because burst-dominated and weakly related bins receive smaller weights. An excessively high threshold would eventually discard usable reference information; the selected value 0.12 is conservative and preserves tracking margin for conditions not represented by S3.

Figure 8 shows the update-performance trade-off controlled by the set-membership factor κ in S1, with the corresponding numerical values reported in Table 4. At κ=0.8, every valid frame is updated and the off-pulse cancellation factor is 11.093 dB. At κ=1.55, the update ratio decreases to 12.3% while the cancellation factor remains 10.404 dB in the one-factor sweep. Larger values further reduce the covariance-update ratio but produce a marked loss of cancellation. Thus κ=1.55 is retained as a balanced setting rather than the value that maximizes a single metric.

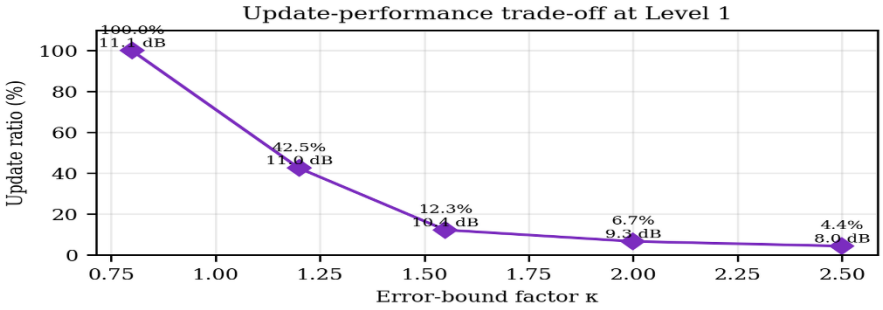

Figure 8. Update-performance trade-off controlled by the error-bound factor in S1

Table 4. One-factor parameter sensitivity results

Study	Value	Coff (dB)	Apeak (dB)	Update ratio
Frame length B	128	11.980	17.607	100.0%
Frame length B	256	11.886	18.386	100.0%
Frame length B	512	11.326	14.351	100.0%
Threshold γmin	0.00	10.362	13.522	100.0%
Threshold γmin	0.12	10.467	13.599	100.0%
Threshold γmin	0.30	10.624	13.740	100.0%
Threshold γmin	0.50	10.717	13.806	100.0%

Study	Value	Coff (dB)	Apeak (dB)	Update ratio
Factor κ	0.80	11.093	21.442	100.0%
Factor κ	1.20	10.995	20.030	42.5%
Factor κ	1.55	10.404	17.205	12.3%
Factor κ	2.00	9.269	15.497	6.7%
Factor κ	2.50	8.015	14.120	4.4%

CG-SM-RSC is most suitable within the simulated operating domain: spectrally concentrated interference, informative auxiliary observations, and channel variation that can be followed by the frame-based recursion. The one-factor sweeps characterize selected operating points rather than a joint optimum or a general guarantee across receiver conditions.

3.4. Discussion

The comparisons suggest two distinct benefits. Coherence gating improves mean cancellation relative to the ungated spectral variants in S2 and S3, where the update ratio remains 100%. Thus, these cases support the reliability-weighting contribution but do not show a reduction in covariance-update frequency. In S1, selective updates provide a performance–adaptation trade-off, with lower cancellation than TD-NLMS and RSC but substantially fewer updated frames. The algorithm should therefore be assessed against the required cancellation level and adaptation budget, rather than a single claim of superiority.

Several issues remain unresolved. Ten runs and three synthetic scenarios provide limited evidence of generalization, and the reported mean differences should not be interpreted as a formal significance test. A target-projection value near zero is a useful indicator but is not a substitute for detection probability, false-alarm rate, or a separate distortion analysis. The current comparisons involve a conventional adaptive baseline and internal spectral ablations, not matched implementations of the recent reconstruction methods [24], [25]. The study therefore establishes a conditional result within its stated simulation design. Measured data, broader statistical evaluation, and implementation measurements are needed before practical performance claims can be made.

4. Conclusion

A coherence-gated set-membership recursive spectral canceller has been evaluated in simulation for pulsed receivers under nonstationary multicomponent interference. It combines guarded spectral identification, frequency-bin reliability gates, a regularized two-reference Wiener solution, continuous synthesis, and residual-driven covariance updates. Among the tested baselines, CG-SM-RSC provides the highest mean off-pulse cancellation in S2 and S3, at 11.852 and 10.563 dB. In S1, it achieves 10.300 dB with a 12.1% covariance-update ratio, while TD-NLMS provides higher cancellation. The results support a condition-dependent trade-off between cancellation and adaptation frequency; they do not demonstrate universal superiority or measured real-time performance.

This study is limited to synthetic observations, ten Monte Carlo runs per scenario, two auxiliary channels, and selected parameter sweeps; no prototype, measured-data validation, runtime measurement, or detection-level evaluation is reported. Performance may deteriorate when both references lose coherence, interference becomes broadly distributed, channel variation exceeds the tracking capability, or target leakage compromises preservation. Future work should test measured receiver data, increase the diversity and number of trials with uncertainty reporting, evaluate detection and target distortion separately, compare additional methods under matched conditions, and assess automatic frame selection, cross-bin regularization, and fixed-point implementation with measured latency and resource use.

CReDiT Author Statement

Vu Quang Luong: Conceptualization, Methodology, Software, Formal Analysis, Writing – Original Draft, Supervision, Project Administration. **Trinh Thi Minh**: Conceptualization, Methodology, Investigation, Formal Analysis, Validation, Writing – Original Draft, Writing – Review & Editing. **Bui Kieu Trong Hoang**: Software, Data Curation, Validation, Visualization, Writing – Review & Editing. All authors have read and approved the final version of the manuscript.

Declaration of Competing Interest

The authors declare that they have no financial or non-financial conflicts of interest, including any personal or institutional relationships that could influence the research reported in this paper.

References

[1] F. Norouzian, A. Pirkani, E. Hoare, M. Cherniakov, and M. Gashinova, "Phenomenology of automotive radar interference," *IET Radar, Sonar & Navigation*, vol. 15, no. 9, pp. 1045–1060, 2021, doi: 10.1049/RSN2.12096.

[2] M. Rameez, M. Dahl, and M. I. Pettersson, "Autoregressive Model-Based Signal Reconstruction for Automotive Radar Interference Mitigation," *IEEE Sensors Journal*, vol. 21, no. 5, pp. 6575–6586, 2021, doi: 10.1109/JSEN.2020.3042061.

[3] M. Rameez, M. I. Pettersson, and M. Dahl, "Interference Compression and Mitigation for Automotive FMCW Radar Systems," *IEEE Sensors Journal*, vol. 22, no. 20, pp. 19739–19749, 2022, doi: 10.1109/JSEN.2022.3204505.

[4] J. Wang, M. Ding, and A. Yarovoy, "Matrix-Pencil Approach-Based Interference Mitigation for FMCW Radar Systems," *IEEE Transactions on Microwave Theory and Techniques*, vol. 69, no. 11, pp. 5099–5115, 2021, doi: 10.1109/TMTT.2021.3090798.

[5] J. Wang, M. Ding, and A. Yarovoy, "Interference Mitigation for FMCW Radar with Sparse and Low-Rank Hankel Matrix Decomposition," *IEEE Transactions on Signal Processing*, vol. 70, pp. 822–834, 2022, doi: 10.1109/TSP.2022.3147863.

[6] S. Chen, P. Stockel, J. Taghia, U. Kühnau, and R. Martin, "Iterative 2D sparse signal reconstruction with masked residual updates for automotive radar interference mitigation," *Eurasip Journal on Advances in Signal Processing*, vol. 2022, no. 1, pp. 33-, 2022, doi: 10.1186/S13634-022-00863-6/FIGURES/12.

[7] Z. Xu and S. Wei, "FMCW Radar System Interference Mitigation Based on Time-Domain Signal Reconstruction," *Sensors 2023, Vol. 23, Page 7113*, vol. 23, no. 16, p. 7113, 2023, doi: 10.3390/S23167113.

[8] L. A. Lopez-Valcarcel, M. Garcia Sanchez, F. Fioranelli, and O. A. Krasnov, "An MTI-Like Approach for Interference Mitigation in FMCW Radar Systems," *IEEE Transactions on Aerospace and Electronic Systems*, vol. 60, no. 2, pp. 1985–2000, 2024, doi: 10.1109/TAES.2023.3345263.

[9] B. P. A. Rohman, A. S. Satyawan, D. Kurniawan, R. Indrawijaya, C. B. A. Wael, and N. Armi, "Robust automotive radar interference mitigation using multiplicative-adaptive filtering and Hilbert transform," *International Journal of Electrical and Computer Engineering*, vol. 14, no. 1, p. 326, 2024, doi: 10.11591/IJECE.V14I1.PP326-336.

[10] Y. Zhou, R. Cao, A. Zhang, and P. Li, "An Interference Mitigation Method for FMCW Radar Based on Time–Frequency Distribution and Dual-Domain Fusion Filtering," *Sensors 2024, Vol. 24, Page 3288*, vol. 24, no. 11, p. 3288, 2024, doi: 10.3390/S24113288.

[11] M. Toth, E. Leitinger, and K. Witrisal, "Variational Signal Separation for Automotive Radar Interference Mitigation," *IEEE Transactions on Radar Systems*, vol. 2, pp. 1007–1026, 2024, doi: 10.1109/TRS.2024.3477353.

[12] M. Yin, B. Feng, J. Yu, L. Li, and Y. Li, "Support Vector Machines Based Mutual Interference Mitigation for Millimeter-Wave Radars," *IET Signal Processing*, vol. 2024, no. 1, p. 5556238, 2024, doi: 10.1049/2024/5556238.

[13] C. Lv, X. Huang, G. Li, and D. Liu, "A Novel Millimeter-Wave Radar Interference Suppression Method Based on VMD and VI-CFAR Algorithms," *International Journal of RF and Microwave Computer-Aided Engineering*, vol. 2024, no. 1, p. 2305711, 2024, doi: 10.1155/2024/2305711.

[14] J. Song, Z. Lu, Z. Xiao, B. Li, and G. Sun, "Optimal Order of Time-Domain Adaptive Filter for Anti-Jamming Navigation Receiver," *Remote Sensing 2022, Vol. 14, Page 48*, vol. 14, no. 1, p. 48, 2021, doi: 10.3390/RS14010048.

[15] E. Gebali, A. ; Landry, A. El Gebali, and R. Landry, "Single and Multiple Continuous-Wave Interference Suppression Using Adaptive IIR Notch Filters Based on Direct-Form Structure in a QPSK Communication System," *Applied Sciences 2022, Vol. 12, Page 2186*, vol. 12, no. 4, p. 2186, 2022, doi: 10.3390/APP12042186.

[16] P. S. R. Diniz, *Adaptive Filtering: Algorithms and Practical Implementation*. Springer, 2019.

[17] J. V. G. De Souza, F. D. R. Henriques, N. N. Siqueira, L. Tarrataca, F. A. A. Andrade, and D. B. Haddad, "Stochastic Modeling of the Set-Membership- Sign-NLMS Algorithm," *IEEE Access*, vol. 12, pp. 32739–32752, 2024, doi: 10.1109/ACCESS.2024.3370439.

[18] M. Djendi and A. Cheffi, "New symmetric decorrelating set-membership NLMS adaptive algorithms for blind speech intelligibility enhancement," *SN Applied Sciences*, vol. 1, no. 12, pp. 1587-, 2019, doi: 10.1007/S42452-019-1641-7/FIGURES/13.

[19] B. Chen, L. Xing, H. Zhao, N. Zheng, and J. C. Principe, "Generalized Correntropy for Robust newline ?Adaptive Filtering," *IEEE Transactions on Signal Processing*, vol. 64, no. 13, pp. 3376–3387, 2016, doi: 10.1109/TSP.2016.2539127.

[20] C. Aydogdu *et al.*, "Radar Interference Mitigation for Automated Driving: Exploring Proactive Strategies," *IEEE Signal Processing Magazine*, vol. 37, no. 4, pp. 72–84, 2020, doi: 10.1109/MSP.2020.2969319.

[21] F. Jin and S. Cao, "Automotive Radar Interference Mitigation Using Adaptive Noise Canceller," *IEEE Transactions on Vehicular Technology*, vol. 68, no. 4, pp. 3747–3754, 2019, doi: 10.1109/TVT.2019.2901493.

[22] S. Chen, J. Taghia, T. Fei, U. Kühnau, N. Pohl, and R. Martin, "A DNN autoencoder for automotive radar interference mitigation," *ICASSP, IEEE International Conference on Acoustics, Speech and Signal Processing - Proceedings*, vol. 2021-June, pp. 4065–4069, 2021, doi: 10.1109/ICASSP39728.2021.9413619.

[23] X. Li *et al.*, "Mitigation of Millimeter-Wave Radar Mutual Interference Using Spectrum Sub-Band Analysis and Synthesis," *Remote Sensing 2023, Vol. 15, Page 3210*, vol. 15, no. 13, p. 3210, 2023, doi: 10.3390/RS15133210.

[24] C. E. Thornton, J. Sloop, S. Brown, A. Orndorff, W. C. Headley, and S. Young, "Temporal Convolutional Autoencoder for Interference Mitigation in FMCW Radar Altimeters," *IEEE Access*, vol. 14, pp. 125062–125073, 2026, doi: 10.1109/ACCESS.2026.3722133.

[25] M. Joshani, B. G. Palm, M. Dahl, and M. I. Pettersson, "Adaptive Interference Mitigation in FMCW Radars Using 2D AR," *IEEE Access*, vol. 14, pp. 39995–40008, 2026, doi: 10.1109/ACCESS.2026.3673034.